RSC Mechanochemistry

ROYAL SOCIETY OF CHEMISTRY

PAPER

View Article Online
View Journal | View Issue

Cite this: *RSC Mechanochem.*, 2025, **2**, 529

Solvent influence on the mechanism of a mechanochemical metal-halide metathesis reaction†

Sourabh Kumar, [a] Dillon Button-Jennings, [b] Timothy P. Hanusa [b] and Ashlie Martini *[a]

Solvents have long been integral to the success of synthetic chemistry, influencing reaction rates, mechanisms, and product selectivity. However, mechanochemistry—typically involving the grinding and mixing of solid reagents—offers an alternative environment that is solvent-free or at least greatly minimizes solvent use, and that drives reactions through mechanical force. In a recent study, the reaction between the salt of a bulky allyl anion, K[A′] (A′ = 1,3-$(SiMe_3)_2C_3H_3$), and a nickel halide gave very different outcomes depending on whether the reaction was conducted without solvent using a solid material, with a starting solvated complex, $[Ni(py)_4Cl_2]$, modified by a small amount of pyridine, or in pyridine solution. Under certain conditions, halide metathesis occurred, forming the allyl complex $[NiA'_2]$ in near quantitative yield. Under others, a redox reaction dominated, generating allyl radicals that coupled and left $\{A'\}_2$ (1,3,4,6-tetrakis(trimethylsilyl)hexa-1,5-diene) as the major product. To understand these differing outcomes, the formation mechanisms of $[NiA'_2]$ under varying solvent conditions were investigated here using Density Functional Theory (DFT). The effects of the reaction conditions on factors such as Gibbs free energy change, bond energy behavior, and transition states collectively suggest that electrostatic stabilization dominates in the solvent phase. In the case of solvate-assisted conditions, a complete energy profile diagram of the reaction between $[Ni(py)_4Cl_2]$ and 2K[A′], leading to $[NiA'_2]$ and KCl, was calculated, with evidence for one of the intermediates ([A′Ni(py)Cl]) being provided by experiments. Calculations confirm that coordination of pyridine to the nickel, whether from the free liquid or (preferentially) from the pyridine solvate, weakens the Ni–Cl bond so that metathesis can proceed easily. If pyridine is absent (*i.e.*, under solvent-free conditions), the redox route will have a kinetic advantage in the reaction. This study provides molecular-level insights for understanding and optimizing solvent-assisted grinding processes.

Received 19th November 2024
Accepted 2nd April 2025

DOI: 10.1039/d4mr00136b

rsc.li/RSCMechanochem

1. Introduction

Reactions induced by mechanical force[1–3] have emerged as green alternatives for synthesizing organic molecules, metal complexes, and advanced materials.[4,5] The mechanical energy required to form such products can often be supplied by well-established milling and grinding techniques.[6] The use of solid-state mechanochemical methods is not a guarantee of synthetic success, however, as some reactions under grinding and milling conditions can be less efficient than solvent-based approaches, resulting in decreased reactivity, lower yields, and possibly different products.[7,8] Interestingly, studies have shown that adding a small amount of solvent during grinding ("liquid-assisted grinding", LAG) can substantially influence the mechanochemical reactivity and the yield of the resulting products.[9] The solvent contribution in grinding or milling conditions, often defined by a volume/mass ratio (η = μL of solvent added/mg of reagents), has been categorized into four distinct regimes: dry (neat) grinding ($\eta = 0$); LAG ($0 < \eta \lesssim 2$); slurries/pastes ($\eta = 2 - 12$); and pure solution-based reactions ($\eta > 12$). The LAG technique has shown promise in speeding up reactions and providing high yields with controlled reactivity, underscoring the importance of solvent optimization in mechanochemical synthesis.

A variation on the LAG technique, in which LAG quantities of solvents are initially present as metal solvates or hydrates, rather than the free liquid, has been termed "solvate-assisted grinding" (SAG).[10] As a result, LAG and SAG are critical adjuncts to mechanochemical synthesis, offering more efficient

[a]*Department of Mechanical Engineering, University of California Merced, Merced, California 95343, USA. E-mail: amartini@ucmerced.edu; sourabhkumar@ucmerced.edu*

[b]*Department of Chemistry, Vanderbilt University, Nashville, Tennessee 37235, USA. E-mail: dillon.a.button-jennings@vanderbilt.edu; t.hanusa@vanderbilt.edu*

† Electronic supplementary information (ESI) available. CCDC 2392374 ($[\{A'NiCl\}_2]$) and 2392373 ([A′Ni(py)Cl]). For ESI and crystallographic data in CIF or other electronic format see DOI: **https://doi.org/10.1039/d4mr00136b**

and sustainable alternatives for synthesizing compounds ranging from pharmaceuticals[11] and organometallic compounds[10] to metal–organic frameworks[12] and covalent organic frameworks.[13]

To study the contribution of solvents in chemical reactions, it is common to compare different solvents' effects on the reaction outcomes.[14] The solvent choice depends on the reaction's aim, but solvents can be usefully classified based on the magnitude of their dielectric constant (ε).[14] The dielectric constant (relative permittivity) of a solvent describes the material's response to an external electric field, and studies have shown that global parameters such as chemical potential and hardness decrease from the gas phase (*i.e.*, solvent-free) to the solvent phase due to the increase in the dielectric constant.[15] The effect of changes in the dielectric constant on mechanochemical synthesis can take various forms, but changes in reaction selectivity are possible outcomes.[16] For example, combining a solvent's dielectric constant (under LAG conditions) with appropriate counter-ion pairing enhanced the selectivity of a Wittig reaction.[17] In another case, the relative polarity (and hence the dielectric constant) of a LAG additive was a key factor in switching the kinetics and chemoselectivity of the reaction between a difluorinated diketone and $(PhS)_2$.[18] A detailed understanding of solvent contributions to mechanochemical reactions will involve evaluating dielectric constants' effects, an area that has been poorly explored in organometallic contexts.

Computational tools are well-suited for exploring the reaction consequences of changes in dielectric constants,[19] and among these, density functional theory[20,21] (DFT) has often been used to explore solution-based methods for synthesizing materials. For example, DFT was used to show that suppression of the collective response of solvent molecules resulted in a decrease in the dielectric permittivity.[22] In another investigation, a combination of DFT and molecular dynamics (MD) simulations was employed to demonstrate that the dielectric constant was influenced by varying temperatures and electrolyte compositions.[23] A recent computational study highlighted the disparities between reactions performed under dry and LAG conditions.[24] In this case, DFT coupled with microkinetic modeling was used to investigate the influence of solvent concentration and the dielectric environment on Diels–Alder reactions and the synthesis of *N*-sulfonylguanidines.

Experimental work can complement computational efforts to analyze solvent effects in mechanochemistry. A recent experimental study systematically compared solvent effects on the synthesis of organometallic complexes under various milling conditions.[10] The synthesis of sterically bulky bis(allyl) complexes $[MA'_2](A' = 1,3\text{-}(SiMe_3)_2C_3H_3)[MA'_2]$ from the binary metal chlorides, MCl_2 (M = Cr, Fe, Co, Ni) and solvated metal chloride complexes, ML_nCl_2 (L = tetrahydrofuran (THF), pyridine) in various conditions, including solvent-free, LAG, SAG (using a pyridine-solvated complex), and pure solution (THF and pyridine) was examined.[10] Two distinct pathways were identified during the reactions, each accompanied by characteristic products. One involved halide metathesis, leading to the formation of $[MA'_2]$ complexes; the other involved a redox process, generating neutral radicals from the starting allyl anions that then coupled to form 1,3,4,6-tetrakis(trimethylsilyl) hexa-1,5-diene ($\{A'\}_2$).

The presence of solvent was found to influence the reaction outcome significantly. It should be noted that in the case of nickel, $[Ni(py)_4Cl_2]$ was the metal solvate used; it provided an amount of pyridine equivalent to $\eta = 0.55$, which is both well within the standard LAG region and is not greatly different from the amount used with separately added liquid pyridine ($\eta = 0.70$). Hence, the LAG/SAG reactions differed primarily in whether the pyridine was initially present as a free liquid or was metal-bound, not in its amount relative to nickel. The results of this study[10] are summarized in Fig. 1, which shows that the $NiCl_2$ reaction with two equivalents of K[A′] led to different proportions of the bis(allyl)metal complex $[NiA'_2]$. The

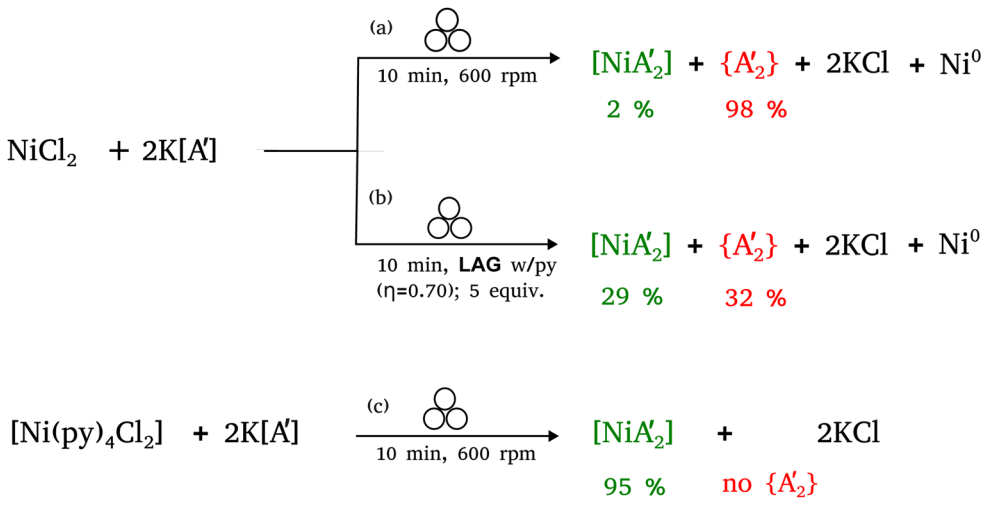

Fig. 1 Reaction schemes for $[NiA'_2]$ synthesis using (a) neat grinding, (b) liquid-assisted grinding (LAG), and (c) solvate-assisted grinding (SAG).[10] The green and red text represent the experimentally observed yields for $[NiA'_2]$ and $\{A'_2\}$, respectively.

underlying reasons for the solvent effect on the reaction outcome remained uncertain, and further investigation is required to explore the mechanisms responsible for this phenomenon. It was unclear, for example, why a pyridine-coordinated nickel complex provided the $[NiA'_2]$ complex with a much greater yield than the equivalent amount of $NiCl_2$ + free pyridine.

In the family of transition metal allyl complexes, those containing nickel were among the first to be synthesized,[25] and nickel derivatives continue to be important in developing high-performance catalysts for olefin polymerization.[26–29] Thus, of the possible systems to study, we focused on the molecular-level reaction mechanism of $[NiA'_2]$ formation under different conditions (solvent-free, in solvents, and using a solvated starting material) using DFT calculations complemented with experimental evidence. This molecular-level approach is a critical first step in understanding larger-scale LAG and SAG processes.

2. Computational details

The model systems described the synthesis of sterically bulky bis(allyl) complex $[NiA'_2](A' = 1,3\text{-}(SiMe_3)_2C_3H_3)$ from the binary metal chloride ($NiCl_2$), and from solvated metal chloride complexes, ML_nCl_2 (L = tetrahydrofuran (THF), pyridine). The computational calculations were performed using the Gaussian 16 quantum chemistry program package.[30] DFT methods were employed at the B3PW91[31] (hybrid GGA density functional)/def2-TZVPP[32,33] level of theory. Dispersion correction *via* Grimme's D3 correction[34] with additional Becke-Johnson damping[35] (*i.e.*, D3(BJ)) method was applied uniformly across all calculations using the "EmpiricalDispersion = GD3BJ" keyword. Tight convergence criteria ("opt = tight" keyword *i.e.*, RMS force criterion to 1×10^{-5}) and an SG1 integration grid ("int(grid = sg1)"), a pruned version of (50 radial shells, 194 angular points per shell) were used to ensure accuracy. The optimized geometries of ground and transition states were subjected to vibrational analysis at the same level of theory, yielding zero and one imaginary frequency, respectively. For Ni(II)-based complexes and structures involved in $\{A'\}_2$ molecule synthesis, both singlet (S_0) and triplet (T_1) spin states were tested for reactants and products. The lowest-energy spin state was adopted for each structure, and the effect of spin state on reaction energetics was systematically analyzed. An implicit solvent model using the Polarizable Continuum Model (PCM) was employed to account for solvation effects, with pyridine and THF as the solvents. The electron localization function (ELF) and electron densities at the bond critical points (BCP) were evaluated using the Quantum Theory of Atoms in Molecules (QTAIM) framework,[36] employing the Multiwfn 3.7 software package.[37]

3. Experimental details

3.1 General considerations

Unless noted otherwise, syntheses were conducted under the exclusion of air and moisture using Schlenk line and glovebox techniques. Proton (^{1}H) and carbon (^{13}C) NMR spectra (Fig. S1–S4†) were obtained at ambient temperature on a Bruker AV-400 MHz spectrometer at 400 and 100 MHz, respectively, and were referenced to the residual resonances of C_6D_6.

3.2 Materials

HCl in dioxane (4 M) was purchased from Sigma Aldrich. $[NiA'_2]$ was prepared according to the literature procedure.[38] [A′NiCl] was prepared from $[NiA'_2]$ and HCl in dioxane as described in the ESI.† Inhibitor-free tetrahydrofuran (THF) and hexanes were degassed and dried by passage through activated alumina columns on an MBRAUN SPS system and then stored over 4A molecular sieves before use. Pyridine was degassed and dried by storage over 50% w/v KOH before use. Deuterated benzene was purchased from Cambridge Isotopes, degassed, and stored over 4A molecular sieves before use.

3.3 Mechanochemical protocol

Planetary milling was performed with a Retsch PM100 mill, a 50 mL zirconia grinding jar, and a safety clamp for air-sensitive grinding. Mechanochemical reactions were run by adding the solid reagents into a grinding jar with approximately 25 g of 5 mm zirconia ball bearings (0.34 g each).

3.4 Synthesis of [A′Ni(py)Cl]

In a typical reaction, [A′NiCl] (0.0107 g, 0.038 mmol) is dissolved in *ca.* 2.5 mL of hexanes in an oven-dried 20 mL glass scintillation vial and sealed under an N_2 atmosphere. To this red solution, 10 μL of pyridine is added dropwise and stirred overnight. The orange solution is slowly evaporated to deposit orange needles of [A′Ni(py)Cl] (0.0117 g, 85%). Anal. calcd for $C_{14}H_{26}ClNNiSi_2$: C, 46.88; H, 7.31; N, 3.91. Found: C, 46.34; H, 7.45; N, 3.45. Proton NMR spectra were unusually broad and difficult to assign, a condition that existed across multiple preparations and solution concentrations. Representative spectra can be found in the ESI (Fig. SI3 and SI4).†

4. Results and discussion

4.1 Steric crowding and electronic effects in $[Ni(py)_4Cl_2]$

The metal halide solvate used in this study is $[Ni(py)_4Cl_2]$, a monomeric complex originally made by the dropwise addition of a heated ethanolic solution of pyridine to an ethanolic solution of $NiCl_2(H_2O)_6$,[39] although it can be generated mechanochemically as well.[10] Its single crystal X-ray structure reveals long Ni–Cl and Ni–N bonds (2.44 Å and 2.13 Å, respectively), which represent 8% and 9% elongations over the sum of the single-bond covalent radii (2.26 Å and 1.95 Å, respectively),[40] and hint at some degree of steric crowding in the molecule.

The level of steric congestion in $[Ni(py)_4Cl_2]$ can be visualized in the encapsulation of the metal coordination sphere. As estimated with the program Solid-G,[41] and in particular by the value of $G_{complex}$ (the net percentage of the coordination sphere covered by the ligands), the value for $[Ni(py)_4Cl_2]$ is high (92.8%) (Fig. 2(A and B)). The observed bond lengthening and inferred steric crowding suggest that the complex may be primed for

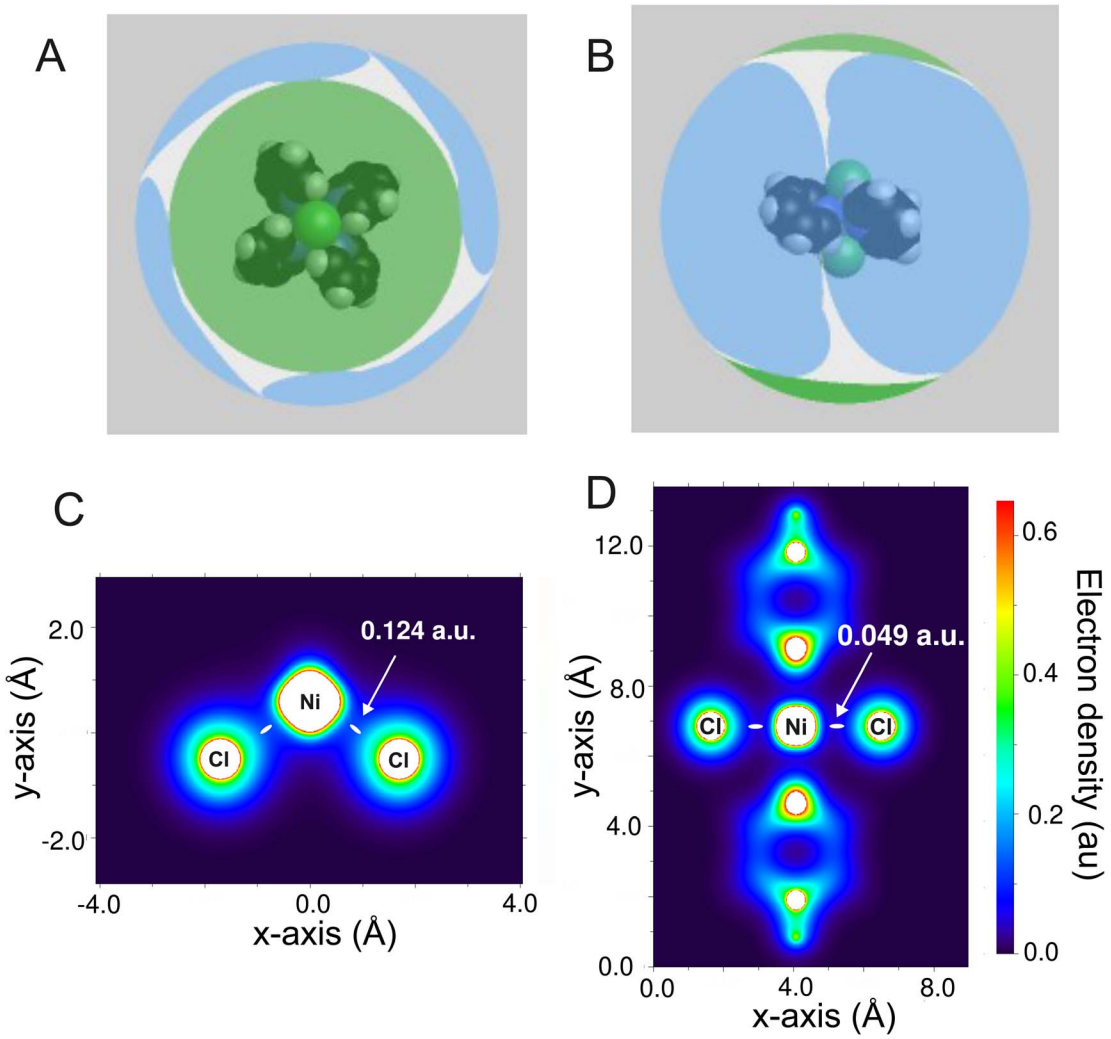

Fig. 2 Visualization of the extent of coordination sphere coverage ($G_{complex}$) of $[Ni(py)_4Cl_2]$: (A) projected down the Cl–Ni–Cl axis; (B) a view from the "side", roughly perpendicular to that in (A). The $G_{complex}$ value represents the net coverage, so any regions of the coordination sphere where the projections of the ligands overlap are counted only once. Electron localization function diagram of (C) $NiCl_2$ and (D) $[Ni(py)_4Cl_2]$. The white points between Ni and Cl electron clouds represent the BCP between Ni and Cl.

ligand dissociation. Moreover, the ELF and electron densities at the BCP were studied for $NiCl_2$ and $[Ni(py)_4Cl_2]$ molecules. As shown in Fig. 2(C), in $NiCl_2$, the ELF plots reveal significant overlap of the outer electron clouds between Ni and Cl atoms, indicating a strong interaction in Ni–Cl bonds. This overlap is absent in $[Ni(py)_4Cl_2]$, where pyridine ligands around Ni reduce electron cloud overlap with Cl (Fig. 2(D)). Additionally, the electron density at the Ni–Cl bond critical point (shown by white points between Ni and Cl atoms) is higher in $NiCl_2$ (0.1243 a.u.) than in $[Ni(py)_4Cl_2]$ (0.0493 a.u.), confirming a stronger Ni–Cl interaction in $NiCl_2$ due to the absence of competing pyridine ligands.

4.2 Formation and structure of [A′Ni(py)Cl]

One of the species identified through computational modeling as a potential intermediate in the formation of $[NiA'_2]$ from K[A′] and $[Ni(py)_4Cl_2]$ is the mono(allyl) complex [A′Ni(py)Cl] (also denoted **IM 4**, see Section 4.3). Although previously unknown, [A′Ni(py)Cl] can be formed from $[\{A'Ni(\mu\text{-}Cl)\}_2]$ (Fig. S5†), itself a new compound generated through the reaction of $[NiA'_2]$ with HCl in dioxane. Slow evaporation of a hexane solution of the compound yields red needles, which allowed its crystal structure to be determined (synthetic and crystallographic details are in the ESI†).

The stoichiometric addition of pyridine into a hexanes solution of $[\{A'Ni(\mu\text{-}Cl)\}_2]$ produces [A′Ni(py)Cl]. Attempts to coordinate additional pyridine molecules by using excess pyridine were not successful. Orange crystals of [A′Ni(py)Cl] were obtained from the slow evaporation of a hexanes solution, and a single crystal X-ray study established its monomeric nature (Fig. 3). The complex displays an η^3-bonded allyl ligand and terminal chloride and pyridine ligands, arranged so that the Cl, N, and C1/C3 carbons of the allyl ligand form a roughly square planar arrangement around the nickel (sum-of-squares error for the least-squares plane through the four atoms = 0.051 Å^2). The TMS groups on the A′ ligand are in a *syn*, *anti*-

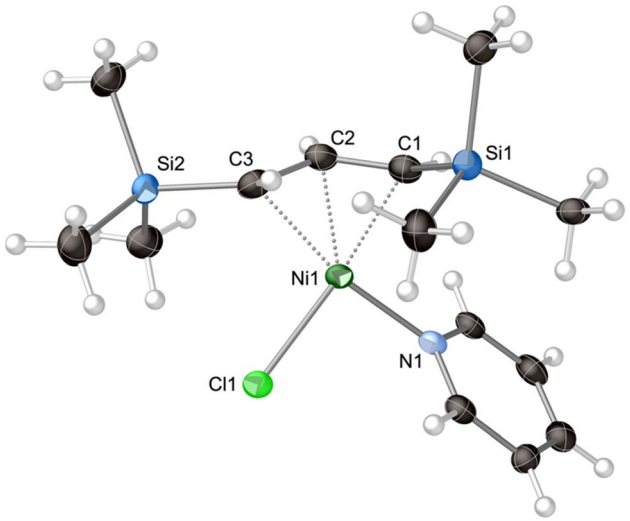

Fig. 3 Thermal ellipsoid plot (50% level) of [A′Ni(py)Cl]. Hydrogens have been assigned an arbitrary radius. Selected bond distances (Å) and angles (deg): Ni1–Cl1, 2.2118(16); Ni1–N1, 1.942(4); Ni1–C1, 2.017(6); Ni1–C2, 1.974(6); Ni1–C3, 2.044(6); C1–C2, 1.402(8); :1.493(8); C2–C3, 1.423(8); C1–Si1, 1.879(6); C3–Si2, 1.861(6); N1–Ni1–Cl1, 95.41(13).

relationship. As is typical for transition metal-bound A′ ligands,[42] the silicon atom of the *syn* substituent (Si2) is deflected somewhat from the C_3 allyl plane toward the nickel atom (0.36 Å). Conversely, the silicon atom of the *anti*-substituent (Si1) is strongly displaced from the C3 plane (0.83 Å), away from the metal center.

4.3 Computational modeling of $[NiA'_2]$ formation

Under ball milling conditions, mechanical activation can enhance the reactivity of solid reactants by breaking bonds and facilitating ion and radical formation.[43] The $\Delta G°$ values for the formation of $[NiA'_2]$ from $NiCl_2$ and K[A′] were calculated at 298.15 K under solvent-free conditions ($\varepsilon = 1.0$) and in pyridine ($\varepsilon = 12.4$) and THF ($\varepsilon = 7.4$) solvents. As demonstrated in Table 1, the $NiCl_2$ + 2K[A′] reaction can exhibit two different product formation outcomes (*i.e.*, $[NiA'_2] + 2KCl$ and $Ni^0 + \{A'\}_2 + 2KCl$) for each environment (with solvents and solvent-free).

Under all conditions examined, the formation of $[NiA'_2] + 2KCl$ products has negative $\Delta G°$ values, indicating the spontaneity of the halide metathesis reaction in the forward direction. Conversely, the positive $\Delta G°$ values associated with the $Ni^0 + \{A'\}_2 + 2KCl$ products formed *via* a redox process imply a non-spontaneous reaction in the forward direction. The solvents' polar nature and their ability to coordinate with metal ions stabilize transition states involved in both reaction types, and the $\Delta G°$ values are more positive under solvent-free conditions (by 10% and 26% for the halide metathesis and redox routes, respectively), although the changes are much larger in absolute terms for the halide metathesis path (roughly 42 and 6 kJ mol^{-1}, respectively).

Table 1 Gibbs free energy change ($\Delta G°$) for possible products from the reaction between $NiCl_2$ and 2K[A′] under solvent-free conditions ($\epsilon = 1.0$), in pyridine ($\epsilon = 12.4$), or in THF ($\epsilon = 7.4$) solvents

Reactants	$\Delta G°$ of possible products (kJ mol^{-1}) at 298.15 K	
$NiCl_2$ + 2K[A′] in	$[NiA'_2] + 2KCl$	$Ni^0 + \{A'\}_2 + 2KCl$
Solvent-free conditions	−370.395	30.684
Pyridine	−412.694	24.046
THF	−411.906	24.803

The dielectric constant under solvent-free conditions and with solvents can affect the Ni–Cl and K–C bond energies and the product formation. We thus examined the bond energies in the different environments. As shown in Fig. 4(A), as the Ni–Cl bond length increases, the energy under solvent-free conditions rises rapidly, reaching a constant value at approximately 400 kJ mol^{-1}. In contrast, the energy increases only up to ~240 kJ mol^{-1} in either solvent. Similarly, in the case of the K–C bond, in Fig. 4(B), the energy remains low in the solvents when compared to the solvent-free phase. This energy disparity indicates that electrostatic stabilization dominates the solvent phase and causes ionic forms to be much more stable in high dielectric constant environments than in the solvent-free phase. This result implies that electrostatic stabilization in the solvent phase could improve milling efficiency compared to solvent-free conditions.

The rupture of the Ni–Cl and K–C bonds will result in the formation of Ni^{2+}, Cl^-, K^+, and $[A']^-$ species, and depending on the experimental milling conditions, reduction of Ni^{2+} to elemental nickel (Ni^0) may also happen. If the latter is the case, concomitant oxidation of the $[A']^-$ anion to the neutral $[A']^\bullet$ radical will occur, and subsequently, two of the $\{A'\}^\bullet$ neutral radicals can combine and form the $\{A'\}_2$ (hexadiene) molecule. Based on transition state search calculations for forming the $\{A'\}_2$ molecule, we explored the reaction's energy profile, which proceeds through a diradical transition state pathway. In our calculations, the dimer $\{A'\}_2$ molecule is assigned a singlet spin state, while A* (radical species) was treated as a doublet. During the transition state, the diradical species (A*–A*) was modeled as a triplet. Fig. 5(A) and (B) show the energy profile diagram of $\{A'\}_2$ formation by the reaction between identical radical molecules for *rac* and *meso* forms. The resulting transition states in the solvent-free phase for the *rac* and *meso* forms of $\{A'\}_2$ are found at the 153.3 and 172.6 kJ mol^{-1} energy barriers, respectively. However, these energy barriers do not change appreciably when solvent is present (*ca.* 2–3% decrease). Hence, there is no significant solvent assistance required for the neutral radicals to combine.

In the previous experimental work, SAG conditions were created by employing the insoluble pyridine solvate complex ($[Ni(py)_4Cl_2]$) during grinding.[10] Computationally, we used the same solvated complex in the triplet (T_1) spin state at the molecular level to study this effect (*cf.* Fig. S6†). The coordinated pyridine moieties donate electron density to the nickel center, weakening the Ni–Cl interaction and adding steric pressure to boost chloride loss. In describing the behavior of the Ni–Cl bond energy for the solvated complex, as shown in Fig. 4(A), it should be remembered that the bonds were already elongated

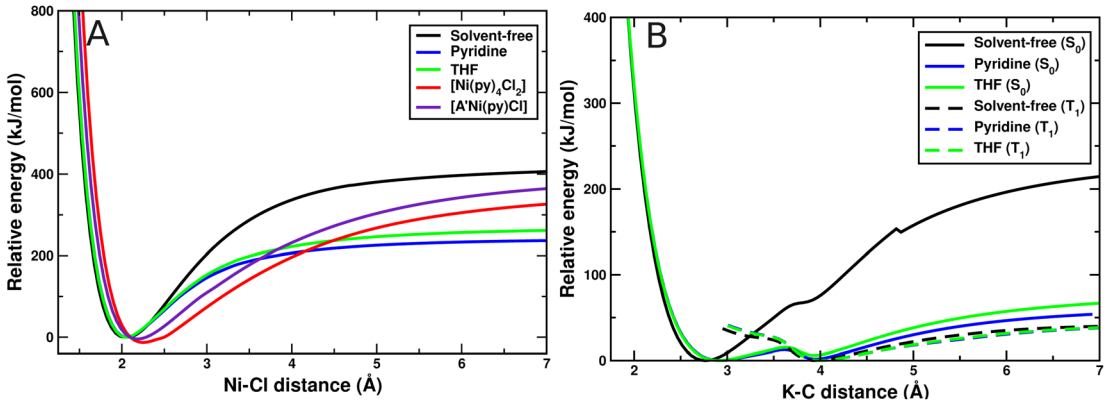

Fig. 4 Bond energy scans for the (A) Ni–Cl and (B) K–C bond as a function of distance. The solvent-free (black curve), pyridine (blue curve), THF (green curve), $[Ni(py)_4Cl_2]$ solvate (red curve), and [A′Ni(py)Cl] solvate (purple curve) in panel A represent the Ni–Cl bond energy curves for the $NiCl_2$ molecule. In B, the solvent-free (black curve), in pyridine (blue curve), and THF (green curve) represent the shortest K⋯C contact in the K[A′] complex. The solid and dashed lines represent the energy at singlet (S_0) and triplet state (T_1), respectively.

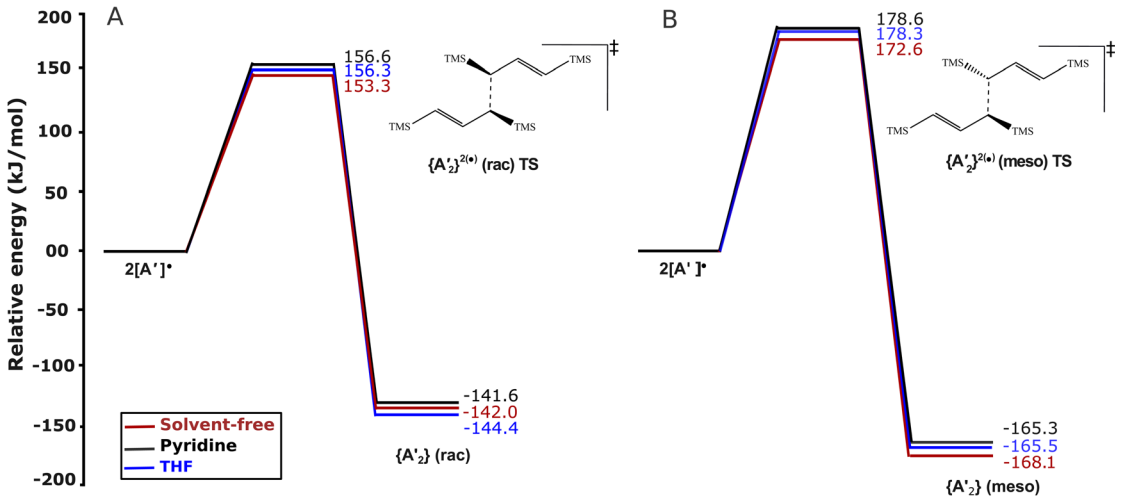

Fig. 5 Energy profile diagram of the synthesis of the $\{A'_2\}$ molecule in *rac* (A) and *meso* (B) forms. The solid red, black, and blue lines represent the case without solvent, with pyridine, and with THF, respectively.

to 2.443 Å compared to the distance in the $NiCl_2$ molecule (2.023 Å).[44] As the bond length increases, the energy rises but remains below that of the $NiCl_2$ molecule in the solvents until *ca.* 4.2 Å. Some caution should be advised in interpreting this finding, given the difference in how the pyridine is modeled with the solvate (explicit pyridine molecules) and the solution (implicit pyridine *via* the dialectic content). Nevertheless, it is clear that the coordination of pyridines in $[Ni(py)_4Cl_2]$ leads to substantial Ni–Cl bond weakening, considerably greater than that in the solvent-free environment.

Fig. 6 shows the computed schematic energy profile diagram illustrating the synthesis of $[NiA'_2]$ from the reaction of the pyridine-solvated complex $[Ni(py)_4Cl_2]$ with 2K[A′]. To facilitate understanding of the reaction mechanism, the process was divided into two steps, introducing a single K[A′] species at each step.

Initially, the reaction begins by forming an intermediate (**IM 1**), accompanied by a modest energy increase (~22 kJ mol^{-1}), attributable to interactions between both molecules (*i.e.*, K[A′] and $[Ni(py)_4Cl_2]$). Subsequently, the formation of an Ni–C bond, and rupture of Ni–Cl and Ni–N bonds causes a substantial energy rise, bringing the system to the first transition state (**TS 1**). The release of the first pyridine ligand and KCl from **TS 1** likely leads to the formation of intermediate **IM 2**. Loss of another pyridine ligand, likely aided by the steric bulk of the η^1–[A′] ligand, leads to the second transition state (**TS 2**). Electron redistribution resulting in the conversion of the initially η^1-bound [A′] ligand to the delocalized η^3-bound conformation culminates in the formation of the intermediate **IM 3**. Further relaxation and pyridine loss occur through transition state **TS 3** followed by intermediate **IM 4** ([A′Ni(py)Cl]).

Subsequently, introducing the second K[A′] species prompts the formation of a fifth intermediate (**IM 5**), accompanied by an energy decrease of approximately 44 kJ mol^{-1} due to interactions between both molecules. Unlike the previous decreasing

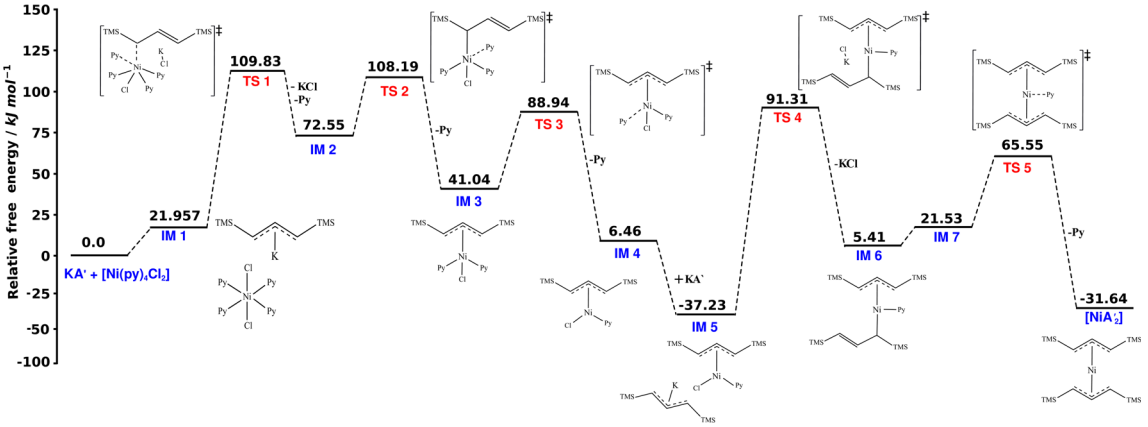

Fig. 6 Schematic representation of the synthesis of the allyl complex [NiA′$_2$] using the pyridine-solvated complex (*i.e.*, [Ni(py)$_4$Cl$_2$]) reaction with 2K[A′]. The **TS 3**, **TS 4** and **TS 5** structures are optimized at the B3LYP level as optimization with B3PW91 was not possible. The final energies reported here are at the B3PW91/def2-TZVPP level of theory. The molecular coordinates are attached in ESI.†

energy trend, the system shows an increase in the energy and progresses through the formation of the fourth transition state (**TS 4**), attributed to the Ni–C bond formation and Ni–Cl bond rupture. The release of the KCl from **TS 4**, associated with the decrease in energy, leads to the generation of the sixth intermediate (**IM 6**). The transition from **IM 6** to the fifth transition state (**TS 5**) involves an energy rise, associated with converting the second [A′] ligand, originally η^1-bound, to the more sterically demanding η^3-bound conformation. Ultimately, the system again releases energy, losing the last pyridine, and yields [NiA′$_2$], exhibiting an overall energy release consistent with the exothermic nature of the reaction mechanism. There is no {A′}$_2$ species in this reaction profile diagram, in agreement with the lack of {A′}$_2$ in the SAG experimental results.

Given these results, it might initially appear inconsistent that under solvent-free conditions, the formation of [NiA′$_2$] is calculated to be spontaneous ($\Delta G° = -370$ kJ mol^{-1}), and the generation of {A′}$_2$ is non-spontaneous ($\Delta G° = +31$ kJ mol^{-1}), even though the experimental production of {A′}$_2$ is almost quantitative and the formation of [NiA′$_2$] is only a trace (Fig. 1). Several factors must be considered to put these results into context. One is that the energy involved in K–C bond cleavage, which makes the allyl anion free for subsequent reaction, is considerably less than that for Ni–Cl scission (Fig. 4). Even in the unsolvated case, the energy of disrupting the K–C interaction is roughly half that of Ni–Cl cleavage, and the difference is greater in the presence of solvents (*e.g.*, in pyridine, the $^{K-C}/_{Ni-Cl}$ energy ratio is roughly one-fourth). This is partially a result of separating the anions from either mono-positive (K^+) or dipositive (Ni^{2+}) centers, so simple charge considerations ($^{Z+Z-}/_r$) would suggest that the former requires less energy. Hence, the availability of the [A′]$^-$ anion is not a critical issue in the reaction scheme, and the differences in reaction outcome must lie in the ease of Ni–Cl bond separation.

A second critical point is that although the coordination of pyridine to $NiCl_2$ weakens the Ni–Cl bond, the coordination process is not immediate under mechanochemical conditions. It has been found that a 10 min grind of $NiCl_2$ with 5 equiv. of pyridine generates a mixture of compounds, primarily [Ni(py)$_4$Cl$_2$] and [Ni(py)$_2$Cl$_2$], the latter being a polymeric subsolvate of $NiCl_2$.[10] Depending on the reagents available, that length of time is sufficient to produce the hexadiene {A′}$_2$ in 98% yield or the [NiA′$_2$] complex in 95% yield (Fig. 1). In solvent-free conditions, and without Ni–Cl bond weakening, the facile separation of the allyl anion from K^+ allows the redox process to start immediately, converting the allyl ligand to its radical form and making it unavailable for reaction with a Ni^{2+} center.

Conversely, when that pyridine is pre-coordinated in the [Ni(py)$_4$Cl$_2$] solvate, Ni–Cl bond cleavage and subsequent metathesis can begin without delay, taking advantage of the generally more favorable free energy condition associated with the metathesis compared to the redox process (Table 1). If pyridine is added as a LAG solvent, however, it takes time for it to coordinate and weaken the Ni–Cl bonds so that metathesis can begin, during which time the redox process can proceed. The result is that provided in Fig. 1B, *i.e.*, both {A′}$_2$ and [NiA′$_2$] form in comparable amounts.

While our study provides valuable insights, certain aspects warrant further consideration to fully capture the complexities of mechanochemical reactions. First, in this study, a continuum solvent model was employed to estimate the influence of solvent on the mechanochemical reaction. This model assumes a homogeneous and infinite solvent environment, which differs from the highly localized and dynamic solvent distributions in ball milling reactions. In ball milling, the solvent often exists as a thin layer on particle surfaces or confined in small cavities, and its distribution is disrupted by mechanical forces. Although the continuum approximation cannot capture these localized effects, it serves as a useful first approximation for evaluating solvent polarity and dielectric effects on reaction energetics.[24] Second, the gas-phase calculations do not fully account for solid-state effects such as lattice stabilization and extended intermolecular interactions. This is a limitation because there are elements of kinetic influence in these reactions that are not fully described with thermodynamic values. Regardless, the calculations reported here offer valuable insights into the

intrinsic thermodynamics of the mechanochemical reactions. These calculations also lay the groundwork for future studies. Such studies may incorporate periodic DFT calculations[45,46] or hybrid quantum-mechanical/molecular-mechanical (QM/MM) approaches that more accurately capture the structural and energetic influences of the solid environment. They may also employ MD simulations with explicit solvent models or coarse-grained approaches that could better capture the localized nature of solvent in ball milling, including its role under LAG conditions and its impact on reaction pathways. Such refinements will bridge computational predictions with experimental outcomes, yielding a comprehensive picture of mechanochemical reactivity.

5. Conclusions

Using DFT methods, we evaluated the potential reasons for the differing reaction outcomes in $[NiA'_2]$ formation from $NiCl_2$ and K[A′] under three distinct environments: solvent-free, in solvents (pyridine and THF), and with a solvated complex. By employing bond energy scans to examine the bond energy behavior and the free energy changes among various products, we determined the reactivity of $NiCl_2$ in both solvent-free conditions and solvents. Furthermore, based on the free energy profile diagram of $[NiA'_2]$, we found that in the pyridine-solvated Ni-complex $[Ni(py)_4Cl_2]$, the reaction is driven by the weakening of Ni–Cl bonds due to electron donation from the pyridine groups; the subsequent rupture of Ni–N bonds is likely facilitated by the bulk of the pyridines and the allyl ligands [A′]. The weakening of Ni–Cl interactions due to pyridine ligands is also evidenced by ELF clouds and electron densities at bond critical points between the Ni and Cl atoms. Ultimately, the reaction's outcome depends on a competition between halide metathesis and a redox reaction, with Ni–Cl bond weakening being crucial to the speed of metathesis and $[NiA'_2]$ formation. A significant advantage of using the $[Ni(py)_4Cl_2]$ complex over simple $NiCl_2$/pyridine LAG is that the solvate provides 'pre-activated' bonds at the reaction's onset, granting the metathesis reaction a kinetic advantage over the competing redox route. When pyridine is introduced as a free liquid (as in LAG), the slower formation of Ni-pyridine bonds permits the redox process to proceed concurrently, generating $\{A'\}_2$ alongside $[NiA'_2]$. Although not specifically examined here, it is highly likely that this analysis is relevant to the related iron system as well.[10] By comparing solvent-free, solvent-based, and solvated complex conditions, this study highlights the role of solvents on the reactivity and stability of intermediates, which is essential for optimizing reaction conditions in synthetic chemistry. The findings provide valuable insights into designing more efficient and selective mechanochemical reactions, particularly in complex organometallic systems.

Data availability

Crystallographic data for the structures have been deposited with the Cambridge Crystallographic Data Centre as CCDC 2392374 ($[\{A'NiCl\}_2]$) and 2392373 ([A′Ni(py)Cl]). Copies of the data can be obtained free of charge on application to CCDC, 12 Union Road, Cambridge CB2 1EZ, UK (fax: (+44)1223-336-033; e-mail: deposit@ccdc.cam.ac.uk).

Conflicts of interest

There are no conflicts to declare.

Acknowledgements

This work was supported by the NSF Center for the Mechanical Control of Chemistry (CMCC), CHE-2303044. The CMCC is part of the Centers for Chemical Innovation Program. The authors thank Prof. Nathan D. Schley (Vanderbilt Univ.) for collecting and solving the crystallographic data for $[\{A'NiCl_2\}]$ and [A′Ni(py)Cl].

References

1 E. M. Gutman, *Mechanochemistry of Solid Surfaces*, World Scientific, 1994.
2 R. Rana, R. Bavisotto, K. Hou, N. Hopper and W. T. Tysoe, *Chem. Methods*, 2021, **1**, 340–349.
3 J. Yeon, X. He, A. Martini and S. H. Kim, *ACS Appl. Mater. Interfaces*, 2017, **9**, 3142–3148.
4 K. J. Ardila-Fierro and J. G. Hernández, *ChemSusChem*, 2021, **14**, 2145–2162.
5 X. Liu, Y. Li, L. Zeng, X. Li, N. Chen, S. Bai, H. He, Q. Wang and C. Zhang, *Adv. Mater.*, 2022, **34**, 2108327.
6 V. Martinez, T. Stolar, B. Karadeniz, I. Brekalo and K. Užarević, *Nat. Rev. Chem.*, 2023, **7**, 51–65.
7 H. Shin, S. Lee, H. S. Jung and J.-B. Kim, *Ceram. Int.*, 2013, **39**, 8963–8968.
8 R. R. Ferreira, A. G. Souza, L. L. Nunes, N. Shahi, V. K. Rangari and D. dos Santos Rosa, *Mater. Today Commun.*, 2020, **22**, 100755.
9 L. E. Wenger and T. P. Hanusa, *Chem. Commun.*, 2023, **59**, 14210–14222.
10 H. P. DeGroot and T. P. Hanusa, *Organometallics*, 2021, **40**, 3516–3525, (the initially reported isolated yield for $[NiA'_2]$ in reaction (c) was 69%. That reaction was conducted in stainless steel jars; a reinvestigation in ZrO_2 equipment found that the yield is now 95%, possibly due to the greater hardness and chemical inertness of ZrO_2 relative to stainless steel. In either stainless steel or ZrO_2, no $\{A'\}_2$ formation was observed (D. Button-Jennings, unpublished results)).
11 P. Ying, J. Yu and W. Su, *Adv. Synth. Catal.*, 2021, **363**, 1246–1271.
12 F. C. Strobridge, N. Judaš and T. Friščić, *CrystEngComm*, 2010, **12**, 2409–2418.
13 G. Das, D. B. Shinde, S. Kandambeth, B. P. Biswal and R. Banerjee, *Chem. Commun.*, 2014, **50**, 12615–12618.
14 W. Morris, E. D. Lorance and I. R. Gould, *J. Phys. Chem. A*, 2019, **123**, 10490–10499.
15 R. Kar and S. Pal, *Int. J. Quantum Chem.*, 2010, **110**, 1642–1647.

16 J. G. Hernández and C. Bolm, *J. Org. Chem.*, 2017, **82**, 4007–4019.
17 K. L. Denlinger, L. Ortiz-Trankina, P. Carr, K. Benson, D. C. Waddell and J. Mack, *Beil. J. Org. Chem.*, 2018, **14**, 688–696.
18 J. L. Howard, M. C. Brand and D. L. Browne, *Angew. Chem. Int. Ed.*, 2018, **57**, 16104–16108.
19 J. J. Varghese and S. H. Mushrif, *React. Chem. Eng.*, 2019, **4**, 165–206.
20 W. Kohn and L. J. Sham, *Phys. Rev.*, 1965, **140**, A1133.
21 P. Hohenberg and W. Kohn, *Phys. Rev*, 1964, **136**, B864.
22 C. Zhang, S. Yue, A. Z. Panagiotopoulos, M. L. Klein and X. Wu, *Phys. Rev. Lett.*, 2023, **131**, 076801.
23 N. Yao, X. Chen, X. Shen, R. Zhang, Z.-H. Fu, X.-X. Ma, X.-Q. Zhang, B.-Q. Li and Q. Zhang, *Angew. Chem. Int. Ed.*, 2021, **60**, 21473–21478.
24 B. S. Pladevall, A. de Aguirre and F. Maseras, *ChemSusChem*, 2021, **14**, 2763–2768.
25 G. Wilke and B. Bogdanović, *Angew. Chem.*, 1961, **73**, 756.
26 M. Chen and C. Chen, *Angew. Chem. Int. Ed.*, 2018, **57**, 3094–3098.
27 M. Xu, F. Yu, P. Li, G. Xu, S. Zhang and F. Wang, *Inorg. Chem.*, 2020, **59**, 4475–4482.
28 T. Liang, S. B. Goudari and C. Chen, *Nature Commun.*, 2020, **11**, 372.
29 R. Zhang, R. Gao, Q. Gou, J. Lai and X. Li, *Polymers*, 2022, **14**, 3809.
30 M. J. Frisch, G. W. Trucks, H. B. Schlegel, G. E. Scuseria, M. A. Robb, J. R. Cheeseman, G. Scalmani, V. Barone, G. A. Petersson, H. Nakatsuji, M. J. Frisch, G. W. Trucks, H. B. Schlegel, G. E. Scuseria, M. A. Robb, J. R. Cheeseman, G. Scalmani, V. Barone, G. A. Petersson and H. Nakatsuji, *et al.*, *Gaussian 16 Rev. C.01*, Gaussian, Inc., Wallingford CT, 2016.
31 A. D. Becke, *J. Chem. Phys.*, 1992, **96**, 2155–2160.
32 F. Weigend and R. Ahlrichs, *PhysChemChemPhys*, 2005, **7**, 3297–3305.
33 D. Rappoport and F. Furche, *J. Chem. Phys.*, 2010, **133**, 134105.
34 S. Grimme, J. Antony, S. Ehrlich and H. Krieg, *J. Chem. Phys.*, 2010, 132.
35 S. Grimme, S. Ehrlich and L. Goerigk, *J. Comp. Chem.*, 2011, **32**, 1456–1465.
36 R. F. W. Bader, *Acc. Chem. Res.*, 1985, **18**, 9–15.
37 T. Lu and F. Chen, *J. Comp. Chem.*, 2012, **33**, 580–592.
38 H. P. DeGroot, I. R. Speight, W. W. Brennessel and T. P. Hanusa, *ACS Org. Inorg. Au*, 2024, **4**, 658–672.
39 G. J. Long and P. J. Clarke, *Inorg. Chem.*, 1978, **17**, 1394–1401.
40 B. Cordero, V. Gómez, A. E. Platero-Prats, M. Revés, J. Echeverría, E. Cremades, F. Barragán and S. Alvarez, *Dalton Trans.*, 2008, 2832–2838.
41 I. A. Guzei and M. Wendt, *Dalton Trans.*, 2006, 3991–3999.
42 K. T. Quisenberry, J. D. Smith, M. Voehler, D. F. Stec, T. P. Hanusa and W. W. Brennessel, *J. Am. Chem. Soc.*, 2005, **127**, 4376–4387.
43 D. Jędrzkiewicz, J. Mai, J. Langer, Z. Mathe, N. Patel, S. DeBeer and S. Harder, *Angew. Chem. Int. Ed.*, 2022, **61**, e202200511.
44 R. E. Bachman, K. H. Whitmire, S. Mandal and P. K. Bharadwaj, *Cryst. Struct. Commun.*, 1992, **48**, 1836–1837.
45 A. M. Belenguer, T. Friščić, G. M. Day and J. K. M. Sanders, *Chem. Sci.*, 2011, **2**, 696–700.
46 S. Lukin, T. Stolar, I. Lončarić, I. Milanović, N. Biliškov, M. d. Michiel, T. Friščić and I. Halasz, *Inorg. Chem.*, 2020, **59**, 12200–12208.